Nanoscale Research Letters

NANO EXPRESS Open Access

Electronic Properties of Armchair Black Phosphorene Nanoribbons Edge-Modified by Transition Elements V, Cr, and Mn

Jiong-Hua Huang[1], Xue-Feng Wang[1,2*], Yu-Shen Liu[3*] and Li-Ping Zhou[1*]

Abstract

The structural, electrical, and magnetic properties of armchair black phosphorene nanoribbons (APNRs) edge-functionalized by transitional metal (TM) elements V, Cr, and Mn were studied by the density functional theory combined with the non-equilibrium Green's function. Spin-polarized edge states introduce great varieties to the electronic structures of TM-APNRs. For APNRs with Mn-stitched edge, their band structures exhibit half-semiconductor electrical properties in the ferromagnetic state. A transverse electric field can then make the Mn-APNRs metallic by shifting the conduction bands of edge states via the Stark effect. The Mn/Cr-APNR heterojunction may be used to fabricate spin *p-n* diode where strong rectification acts only on one spin.

Keywords: Black phosphorene nanoribbons, Half semiconductor, Spin diode, Semiconductor-metal transition, Edge functionalization

Introduction

The discovery of graphene [1, 2] has set off a surge of research for two-dimensional (2D) crystal materials [3–6]. In the last decade, hexagonal boron nitride, transition metal dichalcogenide, black phosphorene, and many others have been prepared or predicted [7–9]. Those 2D materials can be implemented in a wide range of fields, important not only for exploring new physical phenomena and performance under the 2D limit, but also for many novel applications in electronic, spintronic, and optoelectronic devices [10–21]. In addition, some properties of two-dimensional materials can be improved after being tailored into one-dimensional (1D) nanoribbons or/and being functionalized [22, 23]. Excellent performance has been observed in field-effect transistors of bottom-up synthesized graphene nanoribbon [24]. Schottky-barrier-free contacts with 2D semiconductors via metal carbide or nitride functionalized by O or OH groups have been predicted [25]. Edge-modified phosphorene nanoflakes have been proposed for highly efficient solar cells [26]. Atomic defects and impurities can be employed to modulate locally the electronic properties for potential applications in magnetism and catalysis [27–29]. Application of external electric field and heterostructures can further manipulate significantly the electronic properties [30–32].

Among those known 2D materials, black phosphorene is one of the few with superior mechanical, electrical, and optical properties for device applications. Since the fabrication of field-effect transistors based on it [9], black phosphorene has been attracting more and more interest. It is a direct semiconductor with modest band gap (≈ 2 eV) and high hole mobility (≈ 1000 cm^2/(Vs)) [33–35], showing a huge application potential in the fields of electronics, optoelectronics, sensors, catalysis, and batteries [36–39]. Similar to graphene, black phosphorene can be cut along two typical directions into zigzag phosphorene nanoribbons (ZPNRs) or armchair phosphorene nanoribbons (APNRs) [40–42]. The first-principles simulation has shown that substitutional doping of transition metal can easily introduce magnetism into phosphorene for spintronic applications [43]. Absorption of transition metals, anchored by defects, might give rise to half-metallic and metallic composite phosphorene systems [44]. It has been predicted that

* Correspondence: wxf@suda.edu.cn; ysliu@cslg.edu.cn; zhoulp@suda.edu.cn
[1]Jiangsu Key Laboratory of Thin Films, School of Physical Science and Technology, Soochow University, 1 Shizi Street, Suzhou 215006, China
[3]College of Physics and Electronic Engineering, Changshu Institute of Technology, Changshu 215500, China
Full list of author information is available at the end of the article

edge modification of transition metal can also modulate greatly the electronic properties of zigzag phosphorene nanoribbons [45]. However, as far as we know, effects of TM passivation on APNRs have not yet been well studied.

In this paper, we focus on the modulation of electronic properties of APNRs functionalized by typical transitional metal elements V, Cr, and Mn, since they introduce larger magnetic moments than the others. The simulations based on the density functional theory show that the half-semiconductor behavior may appear and can be controlled by a transverse electric field. In addition, high-performance spin *p-n* junction may be designed for spintronic applications [46].

Systems and Computational Methods

Black phosphorus is a layered material in which the atomic layers are stacked together by weak inter-layer van der Waals force while the atoms in each layer are bound by strong covalent bonds. It can be easily peeled off into monolayer phosphorenes. The top view of a phosphorene is schemed in Fig. 1a with a zoom-in part on its right-hand side to show the geometry parameters. Two side views along the armchair and zigzag directions, respectively, are given besides. Each phosphorus atom is bonded to three adjacent phosphorus atoms (with lattice constants 3.31 and 4.38 Å, bond length 2.2 Å, bond angle 96.34°, and dihedral angle 102.1°) to form a pleated honeycomb structure [47]. Like other two-dimensional materials of hexagonal honeycomb lattice such as graphene and molybdenum disulfide, a phosphorene can be tailored to nanoribbons with two typical edge morphologies, the armchair and zigzag black phosphorene nanoribbons [40, 41, 48, 49].

Here, we consider the semiconductor *n*-APNRs for odd width number *n* with mirror symmetric cross section. Similar results should follow for even *n* since the two edges of nanoribbon are almost independent as addressed in the following. The effects of edge modifications by three typical transition metal (TM) elements V, Cr, and Mn are analyzed systematically. As illustrated in Fig. 1b, a TM atom may be adsorbed to an APNR edge on the hollow position (case A) or on the top position (case B). Since case A has a much bigger binding energy, we adopt it where a TM atom is adsorbed near the center of each hollow position and bonds to the two

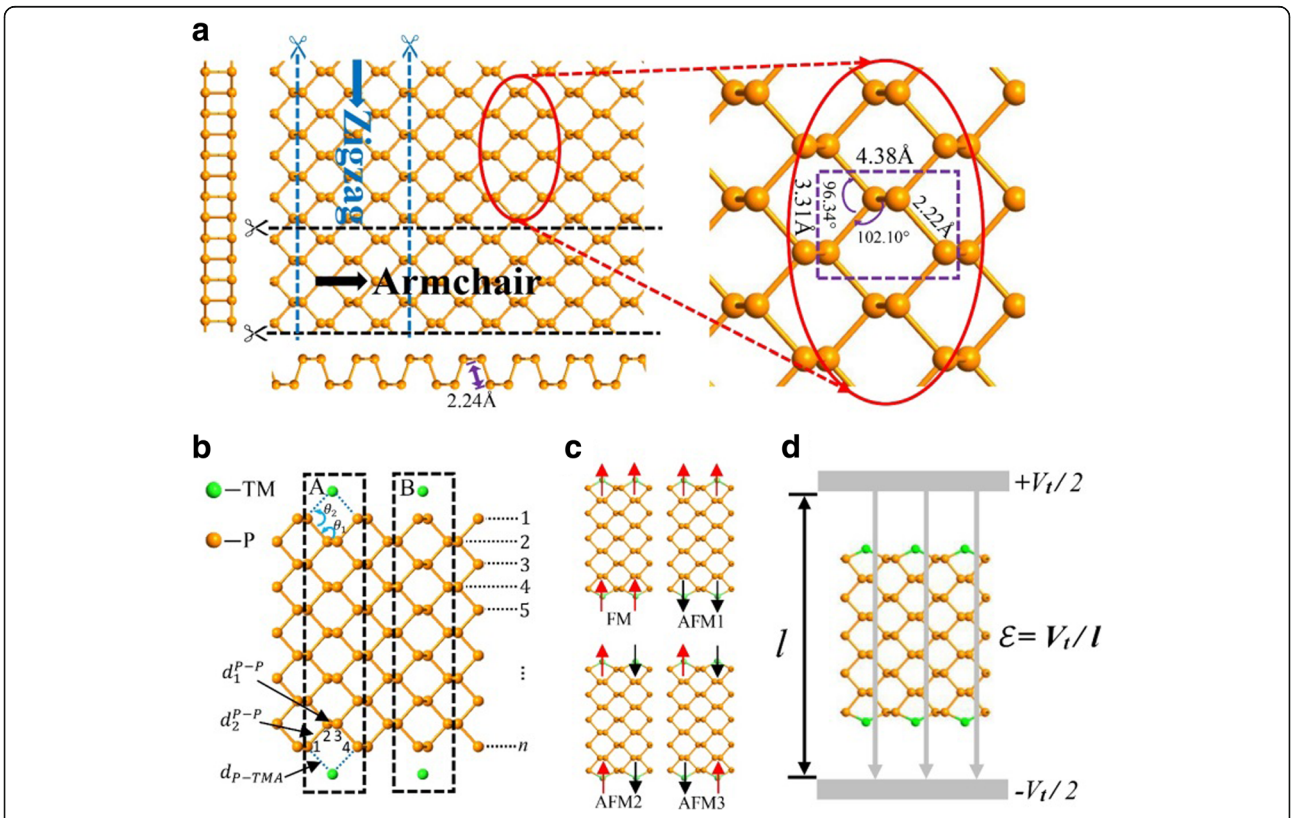

Fig. 1 **a** Top and side views of a 2D phosphorene with a zoom-in view on the right-hand side. The cross-sectional views from the armchair and zigzag edges are shown below and on the left-hand side, respectively. **b** An APNR with TM adatoms at hollow sites (A) and top sites (B) on edge. The dashed frames indicate the size of primitive cell, and the number *n* denotes the width of nanoribbon. **c** The four magnetic configurations of APNRs. **d** The schematic diagram in the presence of a transverse electric field

phosphorus edge atoms besides. To facilitate describing the binding geometry of the TM atoms on the APNR edges, as illustrated in Fig. 1b, we denote the phosphorus atoms at sites 1, 2, 3, and 4 as P_1, P_2, P_3, and P_4, respectively. We define also a few geometry parameters: the bond lengths d_1^{P-P} (between P_2 and P_3), d_2^{P-P} (between P_1, P_2 or P_3, P_4), and d^{P-TM} and the bond angles θ_1 (between d_1^{P-P} and d_2^{P-P}) and θ_2 (between d_2^{P-P} and d^{P-TM}). Due to the magnetism of the TM adatoms, there are four possible magnetic configurations, i.e., FM, AFM1, AFM2, and AFM3 as shown in Fig. 1c. In the absence of magnetic field, our simulation shows that the energy of the AFM2 unit cell in Fig. 1c is about 0.2 eV lower than that of the FM one. The two edges are almost independent, and opposite spin polarization between them in the AFM1 and AFM3 configurations can reduce the energy by an amount less than 0.002 eV. In this paper, we study electronic properties of the nanoribbons in the FM configuration since an applied magnetic field may keep them so. We study also the effects of an applied transverse electric field, as illustrated in Fig. 1d, on the electronic structure and properties of FM APNRs. Finally, we propose possible device applications of the materials.

The transport properties of a nanoribbon junction are calculated by establishing two-probe device structure. The junction is partitioned into three parts: A scattering region, where the junction interface is located, is sandwiched between the left (L) and the right (R) electrodes. When a voltage bias V_b is applied between the two electrodes, we set the Fermi energies in electrodes L and R as $\mu_L = -e|V_b|/2$ and $\mu_R = e|V_b|/2$. The electronic current of spin σ through the quantum devices is evaluated by the Landauer-Büttiker formula [50]:

$$I_\sigma = \frac{e}{h}\int_{-\infty}^{\infty} T_\sigma(E)[f(E-\mu_R)-f(E-\mu_L)]dE \quad (1)$$

Here, $T_\sigma(E)$ is the transmission of spin σ and f the Fermi-Dirac distribution function.

The simulation is performed by the Atomistix toolkits (ATK) package based on ab initio density functional theory (DFT) combined with the non-equilibrium Green's function (NEGF) method [51, 52]. Before the electronic structure and the transport simulations, the structures are optimized until the forces acted on each atom are less than 0.02 eV/Å. We use the spin-dependent generalized gradient approximation with the Perdew-Burke-Emzerhof parametrization (SGGA-PBE) for the exchange-correlation functional. We have confirmed that SGGA+U simulations lead to the same result as presented in the following [43]. A basis set of double zeta-polarized (*dzp*) atomic orbitals is used in the calculation to obtain accurate result. A 20-Å-thick vacuum layer is inserted between neighbor nanoribbons to avoid inter-ribbon couplings. The truncation energy for the base vector expansion of wave functions is set as 150 Hartree or 4082 eV with a *k*-space mesh grid of 1 × 1 × 101. An electronic temperature of 300 K is adopted in the technique of the real-axis integration for the NEGF scheme to facilitate the simulation. The four magnetic configurations are obtained by initially setting the corresponding spin polarizations of the TM adatoms before optimization. The transverse electric field ε is generated by two parallel virtual metal plates, separated by a distance l, with an electric potential difference V_t so $\varepsilon = V_t/l$.

Results and Discussion

Geometry and Binding Energy

In pristine APNRs, the edge P atoms shift to the hollow position so each edge "armchair" becomes narrower comparing to their 2D counterpart, as shown in Fig. 2a, b. If an APNR is hydrogenated with the suspending bond of each edge P atom saturated by one H atom as addressed in Ref. [48, 53], the edge P atoms recover to their 2D positions as illustrated in Fig. 2c. When a TM atom is adsorbed on each hollow position, it passivates the two edge P atoms besides. The armchairs then recover partially, and the edges become magnetized due to the spin polarization of the TM adatoms. In the FM configuration, no reconstruction is observed on the edges and the length of primitive cell remains unchanged as indicated in Fig. 2d–f.

In Table 1, we list the geometry parameters and the binding energy E_b for pristine, hydrogenated, and TM-adsorbing 9- and 17-APNRs in the FM configuration if applicable. Here, $E_b = (mE_X + E_{APNR} - E_{X-APNR})/m$ with E_X, E_{APNR}, and E_{X-APNR} the total energies of an external atom, a primitive cell of pristine APNR, and a primitive cell of APNR passivated by m external atoms, respectively, with $m = 4$ for H and $m = 2$ for TM elements. When we cut a 2D phosphorene to make an APNR, the suspending bonds on edge reduce significantly θ_1 from 102 to 87°. The passivation of the suspending bonds by external atoms recovers θ_1 and introduces a repulsive reaction, marked by the stretch of d_{P-P}^1 and d_{P-P}^2. In the TM cases, the adsorption of V atoms shows the strongest repulsive reaction with the largest θ_1. Similar to that of H, the adsorption of TM element is energetically stable with a binding energy in the order of 4 eV. The two edges of APNRs are almost independent from each other, so the geometry parameters and E_b are insensitive to the width of APNR. The binding geometry and energy hold also in different magnetic configurations for TM-*n*-APNRs.

Electronic Structure and Magnetic Properties

In Fig. 3, we present the band structures and typical wave functions of electrons in 9-APNRs with and without

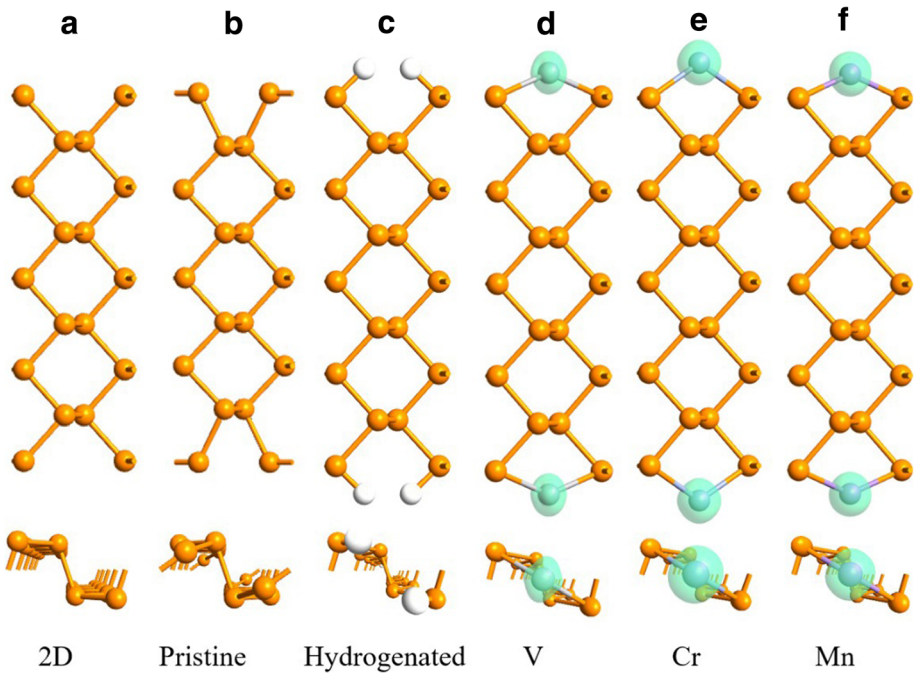

Fig. 2 Geometries of FM 9-APNRs **a** just cut from a 2D phosphorene, **b** geometrically optimized (pristine), **c** hydrogenated, and after adsorbing **d** V, **e** Cr, and **f** Mn atoms on edge. The density of spin polarization of the atoms is shown by the green isosurface at the value of 0.004 e/Å^3

edge modification. Pristine APNRs are non-magnetic indirect semiconductor with a band gap of $E_g \approx 0.5$ eV, where the electronic states on the valence (conduction) band top (bottom) are bulk (edge) states. When the edge P atoms are passivated by H atoms, the conduction band due to edge suspending bonds in pristine APNRs shift away from the band gap and the hydrogenated ANPRs become direct semiconductor with a wider band gap of $E_g \approx 1.0$ eV. The states at the conduction band bottom and on the valence band top are all bulk states. As the width increases from $n = 9$ to 17, the band gap decreases slightly from 1.01 to 0.89 eV in agreement with those predicted by Han et al. [49].

When TM atoms are adsorbed on the edges of APNRs, they remain spin polarized. In the FM configuration, V-*n*-APNRs are magnetic semiconductors with spin-dependent band gap. As illustrated in Fig. 3b, for $n = 9$, the spin-up electrons have an indirect gap of $E_g^{\mathrm{up}} \approx 0.03$ eV while the spin-down electrons have a direct gap of $E_g^{\mathrm{down}} \approx 0.5$ eV. The electronic states in the spin-up

Table 1 The geometry parameters and the binding energy of pristine and modified *n*-APNRs for $n = 9$ and 17 are listed with those of 2D structure. The FM configuration is assumed for TM-modified APNRs

	n	d_1^{P-P}(Å)	d_2^{P-P}(Å)	d^{P-TM} (Å)	θ_1 (degrees)	θ_2 (degrees)	E_b (eV)
2D		2.244	2.225	–	102.10	–	–
Pristine *n*-APNRs	9	2.251	2.253	–	87.01	–	–
	17	2.251	2.253	–	86.96	–	–
H-*n*-APNRs	9	2.263	2.242	–	102.35	–	4.154
	17	2.262	2.242	–	102.33	–	4.154
V-*n*-APNRs	9	2.329	2.287	2.358	102.72	74.41	3.974
	17	2.330	2.290	2.358	102.69	73.98	3.975
Cr-*n*-APNRs	9	2.276	2.271	2.449	99.96	85.56	4.022
	17	2.277	2.271	2.448	100.02	85.58	4.025
Mn-*n*-APNRs	9	2.326	2.304	2.329	101.47	76.08	3.745
	17	2.326	2.303	2.329	101.46	76.13	3.746

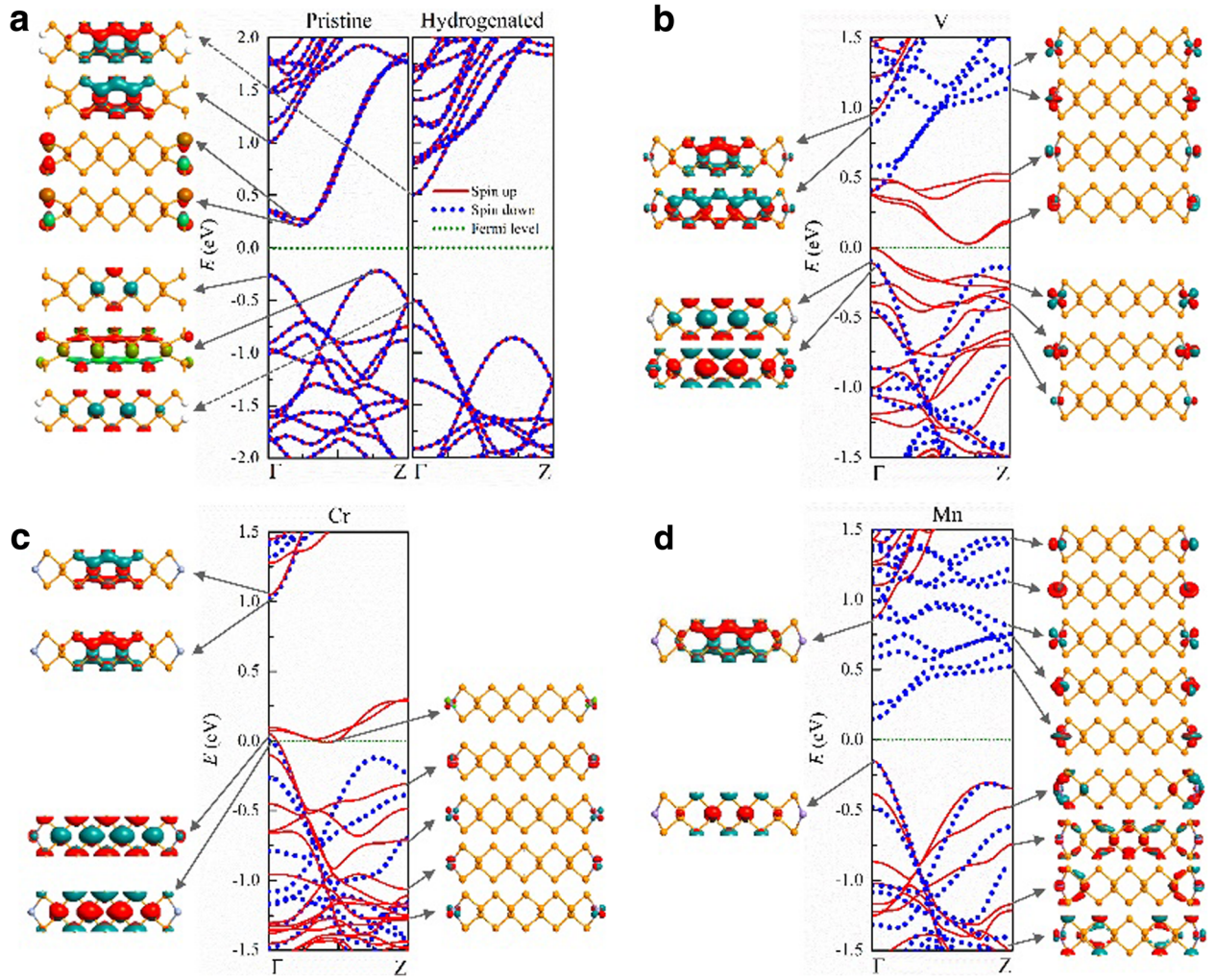

Fig. 3 Band structures and typical wave functions near the Fermi energy of pristine 9-APNRs edge-modified by **a** H, **b** V, **c** Cr, and **d** Mn atoms

bands around the Fermi energy are composed of *d* orbitals of the V adatoms and are confined on edges. Those spin-up edge bands have similar dispersion and are partially occupied. The corresponding valence band top and conduction band bottom separate in the *k* space but are close to each other in energy. A narrow indirect band gap appears for spin-up electrons. In contrast, all the spin-down edge bands are far above the Fermi energy. The spin-down valence band is from bulk states and has opposite dispersion of the spin-down conduction band which is from edge states. This results in the direct band gap for spin-down electrons. The V edge bands appear in pair due to the weak coupling between the left and right edge V atoms. Three of the five pairs are occupied so each primitive cell has a magnetic moment of 6 μ_B.

One pair spin-up and all the spin-down *d* orbital edge bands are located above the Fermi level in Cr-9-APNR as illustrated in Fig. 3c, because there are four *d* orbital electrons in each Cr atom. Due to the slight overlapping of the two highest pairs of spin-up edge bands near the spin-down valence band top, it becomes a half metal with the Fermi level just above the top of the spin-down valence band. In Mn-9-APNR, all the five pairs of spin-up *d* orbital bands are occupied while the spin-down *d* orbital bands are empty as shown in Fig. 3d. It becomes a half semiconductor where the band gaps of opposite spins differ greatly, with $E_g^{\mathrm{up}} \approx 1$ eV for spin-up and $E_g^{\mathrm{down}} \approx 0.3$ eV for spin-down. Both spins have the same valence band top on which are bulk states. However, the conduction band bottom of spin-down is much lower than that of spin-up due to the unoccupied spin-down edge states.

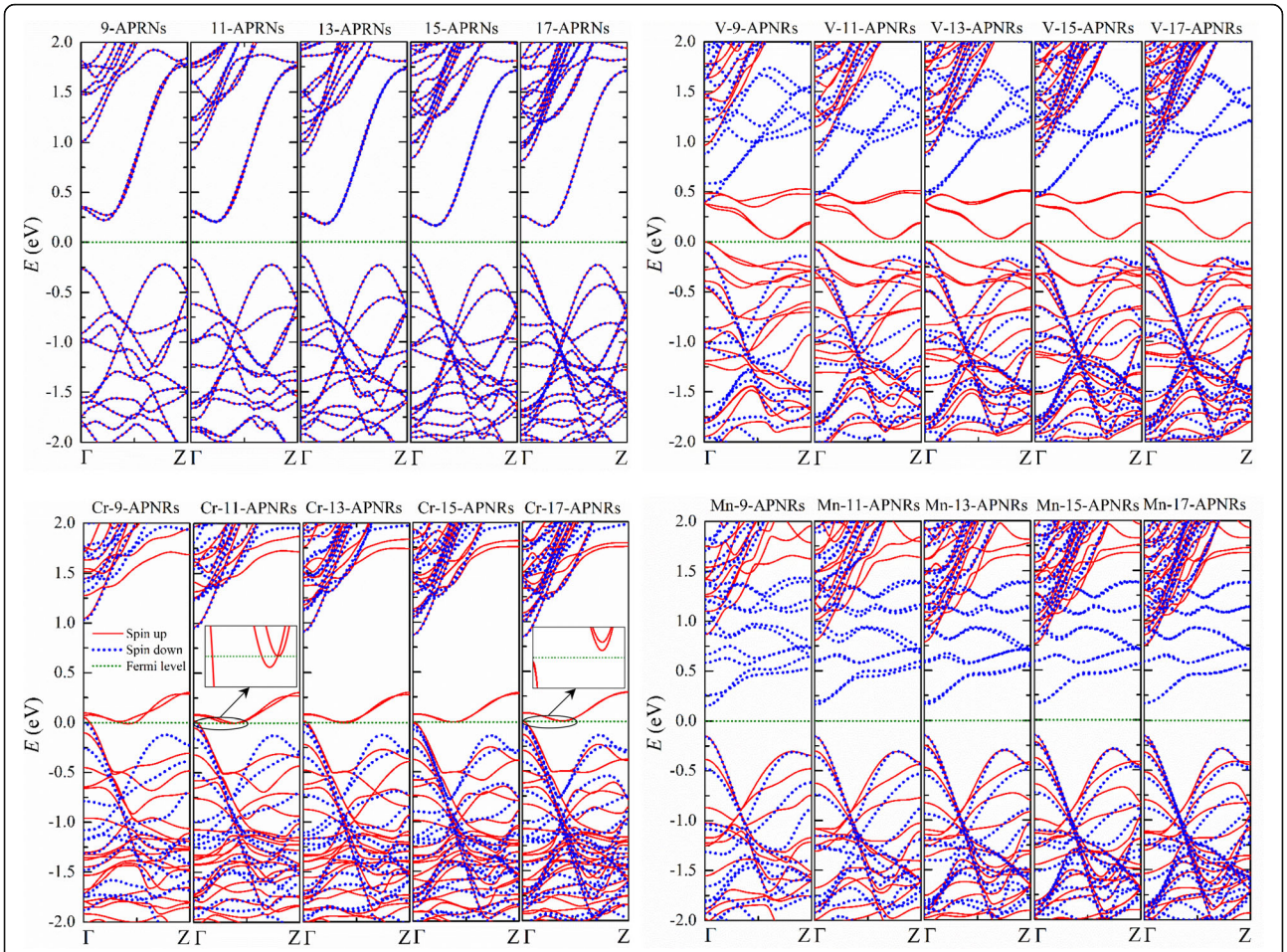

Fig. 4 Band structures of pristine *n*-APNRs and those edge-modified by V, Cr, and Mn atoms for various *n*. Zoomed views of Cr-*n*-APNRs near the Fermi level are shown in the insets for $n = 11$ and 17

The electronic structures of TM-*n*-APNRs remain the same pattern and do not change much as n increases as illustrated in Fig. 4. Nevertheless, the physical properties may vary significantly in the Cr passivated samples because an energy gap may open as n increases. Narrow Cr-*n*-APNRs are half metal, but wide Cr-*n*-APNRs may become semiconductor as shown in the insets of Fig. 4 for $n = 11$ and $n = 17$, respectively.

The magnetic moment distribution profiles of FM TM-9-APNRs are shown in Fig. 2, where the isosurfaces of the spin density $\Delta\rho = \rho^{\mathrm{up}} - \rho^{\mathrm{down}} = 0.004\ \mathrm{e/\AA^3}$ are plotted. Here, ρ^{up} and ρ^{down} are the densities of spin-up and spin-down electrons, respectively. The magnetic moments are concentrated mainly around the TM atoms, and the contribution from the P atoms is too small to be shown clearly. In Table 2, we present the total magnetic moment M_{T} in a primitive cell, the moment sum of the ten edge atoms $M_{\mathrm{E}} = 2\,M(\mathrm{TM}) + 4\,M(\mathrm{P_1}) + 4\,M(\mathrm{P_2})$, and the moment of a single edge atom TM, $\mathrm{P_1}/\mathrm{P_4}$, or $\mathrm{P_2}/\mathrm{P_3}$.

The total magnetic moments come mainly from the edge atoms ($M_T \approx M_E$) and in unit of μ_{B} per primitive cell are close to the valence electron numbers of the transition metal atoms minus 4. In V-*n*-APNRs, the edge P atoms ($\mathrm{P_1}$ and $\mathrm{P_4}$) are antiparallelly polarized slightly while the second edge P atoms ($\mathrm{P_2}$ and $\mathrm{P_3}$) are parallelly polarized. So the magnetic moments of the P atoms are almost canceled with each other. Each V atom has a

Table 2 The total (M_{T}), edge (M_{E}), and single-atom magnetic moments in unit of μ_{B} per primitive cell in TM-*n*-APNRs for $n = 9$ and 17

	n	M_{T}	M_{E}	M (TM)	M ($\mathrm{P_1}$)	M ($\mathrm{P_2}$)
V-*n*-APNR	9	6.012	5.790	3.045	− 0.082	0.007
	17	6.006	5.770	3.035	− 0.082	0.007
Cr-*n*-APNR	9	8.082	8.174	4.673	− 0.270	− 0.023
	17	8.061	8.172	4.672	− 0.269	− 0.024
Mn-*n*-APNR	9	9.996	9.792	4.748	0.003	0.071
	17	9.998	9.794	4.749	0.003	0.071

magnetic moment of about $3\,\mu_B$ from three $3d$ orbitals. The $4s$ orbital is fully occupied similar to a single V atom. In contrast, the edge P atoms in Cr-n-APNRs have much larger magnetic moments of M (P1) $\approx -0.27\mu_B$. Coincidently, they have the longest d^{P-TM} among the three TM-APNRs, indicating also the greatest geometry deviation of the P atoms from those in 2D phosphorene. Furthermore, each Cr atom has a magnetic moment of approximate $5\,\mu_B$, instead of $4\,\mu_B$. This suggests that its $4s$ orbital is not fully occupied and contributes to spin polarization, similar to the case of isolated Cr atom having a valence electron configuration of $3d^5 4s^1$. The spin-polarized s orbitals of Cr atoms in Cr-APNRs might have induced the antiparallel spin polarization in the p orbitals in their neighbor P atoms via the kinetic exchange mechanism. In Mn-n-APNR, the d orbitals of Mn atom are half occupied with a magnetic moment of about $5\,\mu_B$ and the neighbor P atoms are all parallelly polarized very weakly. In Fig. 5, we plot the partial density of states (PDOS) (blue) of d orbitals in TM atoms together with the total density of states (DOS) (black) of 9-APNRs. Here, the spin split and the energy spread of d orbitals are shown clearly. In pristine and hydrogenated APNRs, spin-up and spin-down DOS spectra overlap with each other indicating no spin polarization. In TM-APNRs, the spin-up and spin-down d orbital PDOS spectra distribute mainly in an energy range of 2 to 4 eV. They are well separated in energy with a separation of about 3, 9, and 4 eV in V-, Cr-, and Mn-APNR, respectively. Excluding the d orbitals, the p orbitals of P atoms dominate the contribution to the DOS of valence bands. Note that the s orbitals of Cr atoms also contribute significantly in Cr-APNRs. Edge passivation of Co and Ni atoms can also introduce magnetism in APNRs, but the magnetism introduced by other TM elements like Sc, Ti, Fe, Cu, and Zn might be quite limited.

Effects of a Transverse Electric Field

Transverse electric field has been widely employed in electronic devices to control the carrier concentration and the band structure of semiconductors [54, 55]. As indicated in Fig. 1d, we simulate the electronic structures of TM-n-APNRs in the FM configuration under a transverse electric field $\mathcal{E} = V_t/l$ parallel to the nanoribbon plane, via sandwiching nanoribbons between two parallel bars. Here, V_t is the voltage difference between the two bars and l is the separation between them. Due to the Stark effect, two degenerate states separated in real space by a distance Δ along the electric field should split by an amount of $\delta E = e\mathcal{E}^*\Delta$, where the effective electric field $\mathcal{E}^*$ is usually smaller than the external electric field $\mathcal{E}$ as a result of the screening effect. In TM-n-APNRs, the distance Δ between the state centers of an edge-band pair can be as much as the nanoribbon width if each state is confined only on one edge but Δ should be shorter or even vanish for mixed edge states. As illustrated by the wave functions in Fig. 3, the edge states are usually mixed.

In Fig. 6, we present the band structures of V-, Cr-, and Mn-13-APNR for various $\mathcal{E}$. The nanoribbon width is about $w = 0.5(n-1) \times 3.31\ \text{Å} + d^{P-TM}\cos(135^\circ - \theta_2) \approx 21$ Å.The

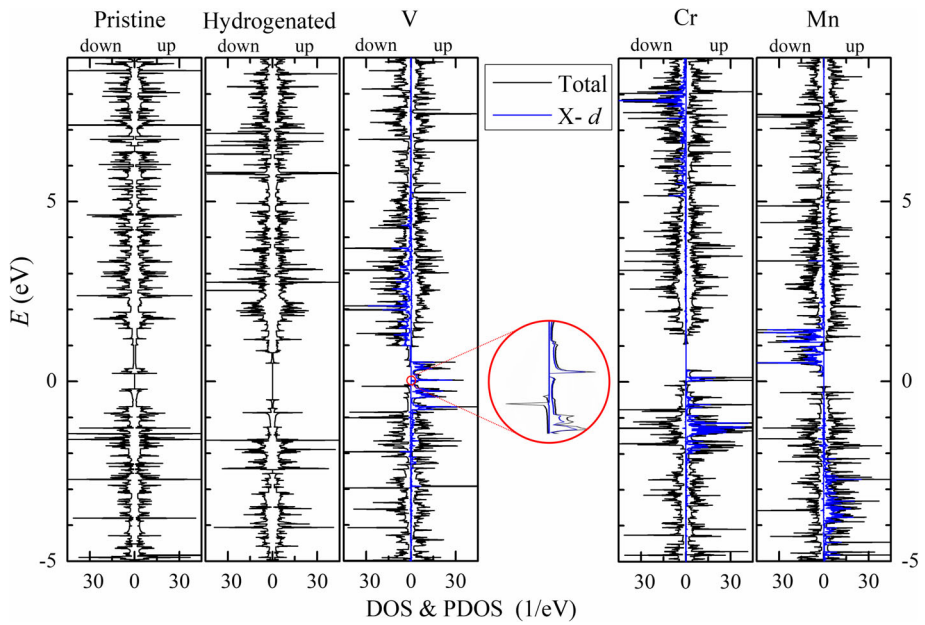

Fig. 5 The DOS (black curve) of pristine and modified 9-APNRs in their FM state is plotted for the up spin (right) and down spin (left). The d orbital PDOS (blue curve) of TM atoms is also presented for comparison. The DOS of V-9-APNR near the Fermi energy is zoomed in the inset to show the band gap

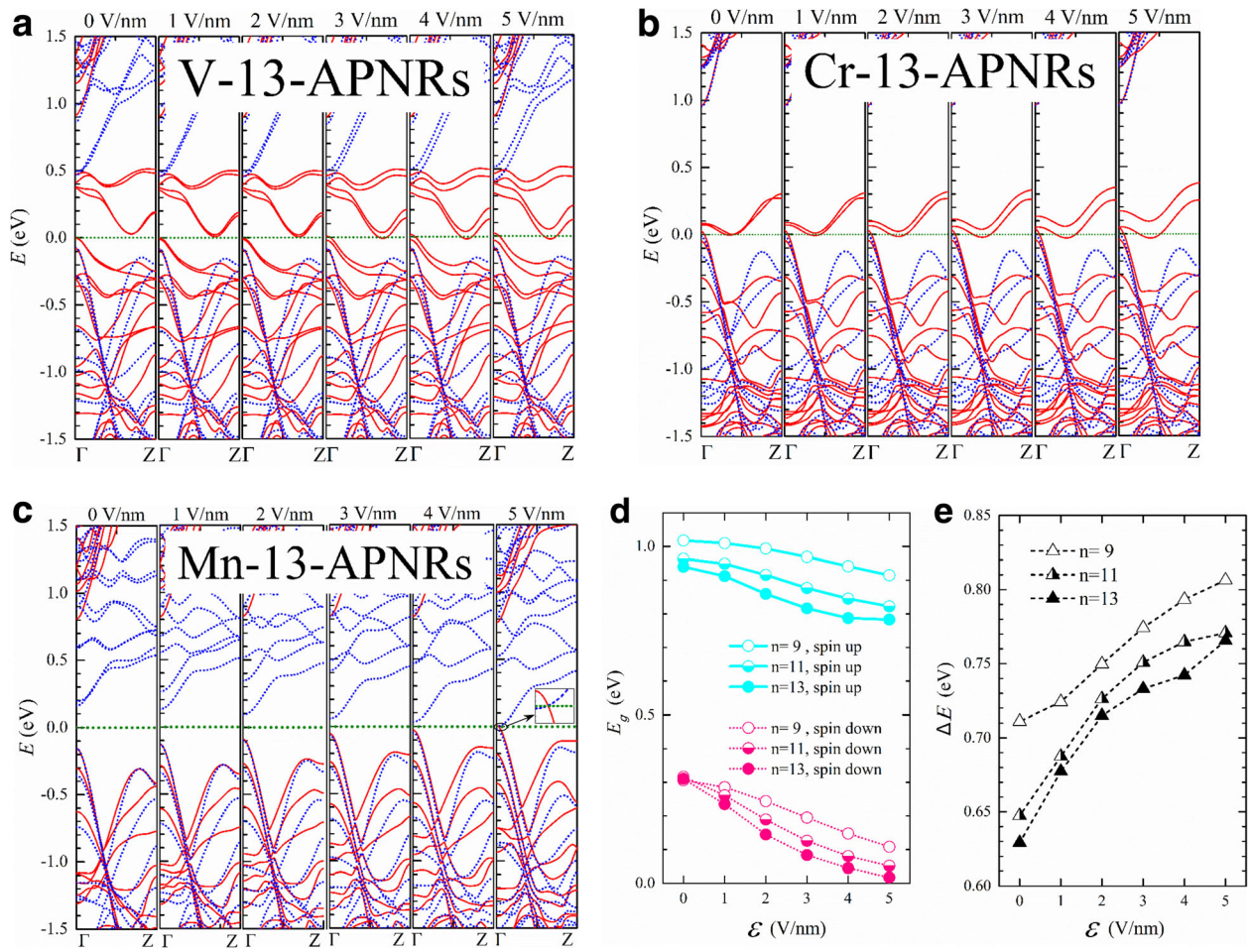

Fig. 6 The spin-up (solid) and spin-down (dotted) band structures of **a** V-, **b** Cr-, and **c** Mn-13-APNRs under a transverse electric field of strength $\mathcal{E} = 0, 1, \ldots, 5$ V/nm. **d** The band gaps of Mn-*n*-APNRs versus $\mathcal{E}$ for up spin (E_g^{up}, solid lines) and down spin (E_g^{down}, dotted lines) with $n = 9$, 11, and 13. **e** The gap difference $\Delta E = E_g^{\text{up}} - E_g^{\text{down}}$ versus $\mathcal{E}$

Stark splitting is much smaller than $e\mathcal{E}w$ indicating strong screening effect or strong mixture of the edge states. Since V-13-APNR has a very narrow spin-up band gap, it becomes half metallic at about $\mathcal{E} = 3$ V/nm. The Stark splitting of conduction edge bands can reach to 0.1 eV at $\mathcal{E} = 5$ V/nm. Cr-13-APNR shows a similar strength of Stark splitting and remains half metallic under the transverse field.

A much stronger Stark effect is observed in the half-semiconductor Mn-13-APNR as shown in Fig. 6c. The spin-down conduction band pairs of edge states get a split of about 0.55 eV at the Γ point in k space under $\mathcal{E} = 5$ V/nm. The spin-down conduction band overlaps with the spin-up valence band, and the Mn-13-APNR transits from a half semiconductor to a metal as illustrated by the zoomed inset. In Fig. 6d, we plot the spin-up and spin-down energy gaps versus the field strength. The electron wave functions change with the field, and the energy gaps do not vary linearly with the field. The band gap of Mn-13-APNRs almost vanishes at $\mathcal{E} = 5$ V/nm for spin-down electrons but remains above 0.75 eV for spin-up electrons. The energy gap difference ΔE between the opposite spins is plotted versus $\mathcal{E}$ in Fig. 6e for $n = 9$, 11, and 13. ΔE increases in a much slower step for $n = 9$ than for $n = 11$ and 13 at the low field, but the manner reverses at the high field.

Spin *p-n* Junction

We have seen that TM atoms can modulate the band structure of APNRs in various ways. This offers opportunities for novel device design. For example, we can combine Cr-APNRs and Mn-APNRs to form a spin-dependent *p-n* junction. Experimentally, metal ion doping [56] in phosphorene is available. Smooth stitching of 2D materials [57] and atomic edge modification of nanoribbons can also be realized [58]. Those techniques might be used to fabricate the *p-n* junction. In Fig. 7a, we plot its current-voltage (*I-V*) characteristic obtained from simulation of the two-probe system shown in the upper inset. The spin *p-n* junction shows very strong rectification effect for spin-up

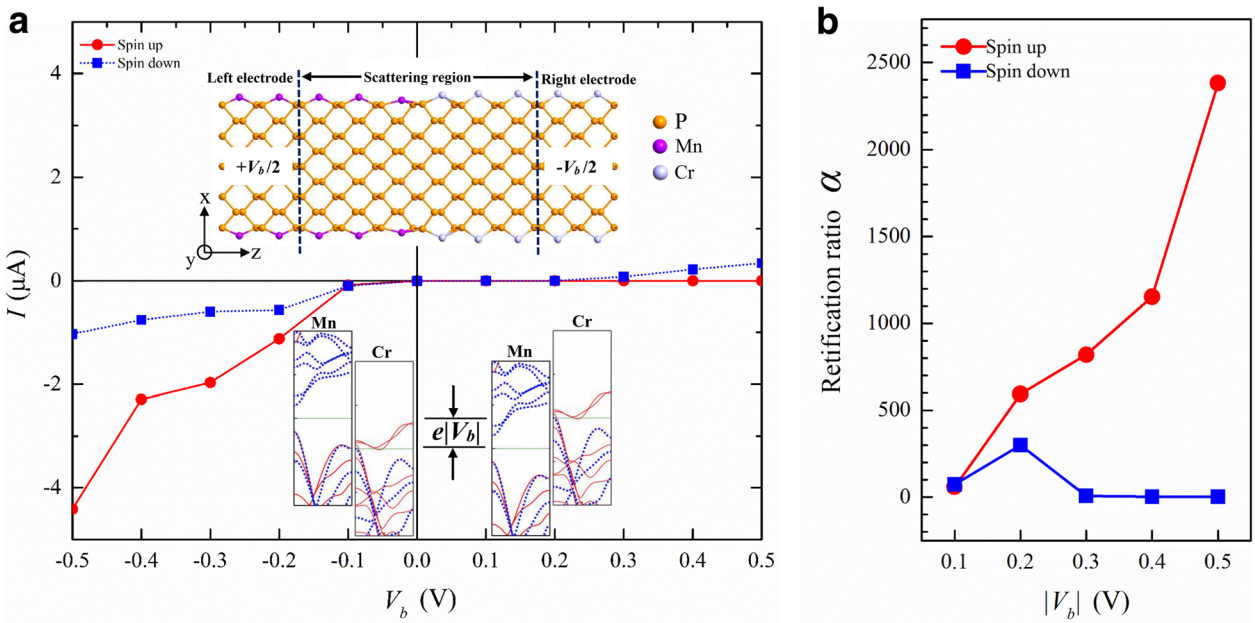

Fig. 7 a The spin-dependent *I-V* characteristic of a Mn/Cr-9-APNR heterojunction. The geometry of the two-probe system is shown in the upper inset. The lower insets scheme the alignments of electrode energy bands for negative and positive biases. **b** The corresponding rectification ratio *a* is plotted versus the bias magnitude

electrons but only weak effect for spin-down electrons. This spin dependence comes from the distinguished band structures of the left and right electrodes as illustrated in the lower inset. Under negative bias, the left Mn-APNR electrode has a Fermi energy $\mu_L = e|V_b|/2$ and the right Cr-APNR $\mu_R = -e|V_b|/2$. Inside the transport window of energy range $[\mu_L,\mu_R]$, there is only a very small part of the spin-down energy band in the Cr-APNR electrode, so the spin-down current remains low. In contrast, a wide overlapping of the spin-up energy bands exists in both Mn- and Cr-APNR electrodes and the spin-up current increases quickly with the bias. Inside the transport window $[\mu_R,\mu_L]$ under positive bias, however, there is no spin-up energy band in the left electrode and the corresponding current remains almost zero since Mn-APNR is a *p*-type wide gap semiconductor for up spin. The spin-down current begins to increase at $V_b = 0.2$ V when the right Fermi energy aligns to the left spin-down conduction band. In Fig. 7b, we plot the rectification ratio $\alpha_\sigma = [I_\sigma(-|V_b|) - I_\sigma(|V_b|)]/I_\sigma(|V_b|)$ of spin σ as a function of the bias magnitude $|V_b|$. At $|V_b| = 0.5$ V, the APNR spin *p-n* junction has a rectification of 2400 for up spin and only 2 for down spin.

Conclusions

The DFT-NEGF simulation suggests that edge functionalization of TM atoms can manipulate greatly the electrical and magnetic properties of non-magnetic semiconductor APNRs and make them metallic or half semiconductor. The TM atoms in TM-APNRs hold their electronic configurations in isolated state where the magnetism of V and Mn atoms comes mainly from *d* orbitals but that of Cr from both *d* and *s* orbitals. In Mn-APNRs, the *d* orbitals are half-filled. All the spin-up *d* orbitals of the Mn atoms are occupied and the spin-down *d* orbitals are above the Fermi level. Due to the narrow band gap of the *d* orbital, Mn-APNRs become half semiconductor where the spin-down energy bands have a much narrower gap at the Fermi level than the spin-up ones. This peculiar property might be employed for spintronic device design since the materials can be semiconductor for one spin and insulator for the other under proper conditions. With the help of Stark effect on edge states, the energy gaps can be further modulated by an applied transverse electric field. For example, a field of 5 V/nm can close the band gap of spin-down electrons while maintain a gap of 0.75 eV for spin-up electrons. Taking advantage of the drastic difference of energy band between Mn- and Cr-APNRs, we can design spin *p-n* diodes of Mn/Cr-APNR junction in which strong rectification occurs only for one spin.

Abbreviations

1D: One dimensional; 2D: Two dimensional; AFM: Antiferromagnetic; APNR: Armchair black phosphorene nanoribbon; ATK: Atomistix toolkits; DFT: Density functional theory; DOS: Density of states; FM: Ferromagnetic; NEGF: Non-equilibrium Green's function; TM: Transition metal

Acknowledgements
This work was supported by National Natural Science Foundation of China (Grant Nos. 61674110, 6167204, and 11274238).

Funding
National Natural Science Foundation of China (Grant Nos. 61674110, 6167204, and 11274238).

Availability of Data and Materials
The datasets supporting the conclusions of this article are included within the article.

Authors' Contributions
XFW conceived the research work. JHH carried out the computation. JHH and XFW wrote the manuscript. All the authors analyzed the results and approved the final manuscript.

Authors' Information
XFW is a professor in the School of Physical Science and Technology, Soochow University. He obtained his BSc degree in 1989 from Shanghai Jiaotong University and earned his PhD degree in 1994 at Shanghai Institute of Microsystem and Information Technology, Chinese Academy of Science. YSL is a professor in College of Physics and Engineering, Changshu Institute of Technology. LPZ is a professor in the School of Physical Science and Technology, Soochow University.

Competing Interests
The authors declare that they have no competing interests.

Publisher's Note

Author details
[1]Jiangsu Key Laboratory of Thin Films, School of Physical Science and Technology, Soochow University, 1 Shizi Street, Suzhou 215006, China. [2]Key Laboratory of Terahertz Solid-State Technology, Chinese Academy of Sciences, 865 Changning Road, Shanghai 200050, China. [3]College of Physics and Electronic Engineering, Changshu Institute of Technology, Changshu 215500, China.

Received: 1 February 2019 Accepted: 3 April 2019
Published online: 27 April 2019

References

1. Novoselov KS, Geim AK, Morozov SV, Jiang D, Zhang Y, Dubonos SV, Grigorieva IV, Firsov AA (2004) Electric field effect in atomically thin carbon films. Science 306:666–669
2. Novoselov KS, Jiang D, Schedin F, Booth TJ, Khotkevich VV, Morozov SV, Geim AK (2005) Two-dimensional atomic crystals. Proc Natl Acad Sci USA 102:10451–10453
3. Xu MS, Liang T, Shi MM, Chen HZ (2013) Graphene-like two-dimensional materials. Chem Rev 113:3766–3798
4. Gupta AS, Seal S, Sakthivel T (2015) Recent development in 2D materials beyond graphene. Prog Mater Sci 73:44–126
5. Tan CL, Cao XH, Wu XJ, He QY, Yang J, Zhang X, Chen JZ, Zhao W, Han SK, Nam GH, Sindoro M, Zhang H (2017) Recent Advances in Ultrathin Two-Dimensional Nanomaterials. Chem Rev 117:6225–6331
6. Feng YP, Shen L, Yang M, Wang AZ, Zeng MG, Wu QY, Chintalapati S, Chang CR (2017) Prospects of spintronics based on 2D materials. WIREs Comput Mol Sci 7:e1313
7. Zhang JT, Xiong ZG, Zhao XS (2011) Graphene-metal-oxide composites for the degradation of dyes under visible light irradiation. J Mater Chem 21: 3634–3640
8. Wang QH, Kalantar-Zadeh K, Kis A, Coleman JN, Strano MS (2012) Electronics and optoelectronics of two-dimensional transition metal dichalcogenides. Nat Nanotechnol 7:699–712
9. Li LK, Yu YJ, Ye GJ, Ge QQ, Ou XD, Wu H, Feng DL, Chen XH, Zhang YB (2014) Black phosphorus field-effect transistors. Nat Nanotechnol 9:372–377
10. Chen X, Yan TF, Zhu BR, Yang SY, Cui XD (2017) Optical control of spin polarization in monolayer transition metal dichalcogenides. ACS Nano 11: 1581–1587
11. Xie L, Liao MZ, Wang SP, Yu H, Du LJ, Tang J, Zhao J, Zhang J, Chen P, Lu XB, Wang GL, Xie GB, Yang R, Shi DX, Zhang GG (2017) Graphene-contacted ultrashort channel monolayer MoS_2 transistors. Adv Mater 29:1702522
12. Gong C, Li L, Li ZL, Ji HW, Stern A, Xia Y, Cao T, Bao W, Wang CZ, Wang Y, Qiu Z, Cava RJ, Louie SG, Xia J, Zhang X (2017) Discovery of intrinsic ferromagnetism in two-dimensional van der Waals crystals. Nature 546:265–269
13. Chen S, Shi GQ (2017) Two-dimensional materials for halide perovskite-based optoelectronic devices. Adv Mater 29:1605448
14. Barati F, Grossnickle M, Su SS, Lake RK, Aji V, Gabor NM (2017) Hot carrier-enhanced interlayer electron-hole pair multiplication in 2D semiconductor heterostructure photocells. Nat Nanotechnol 12:1134–1139
15. Mendoza-Sánchez B, Gogotsi Y (2016) Synthesis of two-dimensional materials for capacitive energy storage. Adv Mater 28:6104–6135
16. Di J, Xia JX, Li HM, Liu Z (2017) Freestanding atomically-thin two-dimensional materials beyond graphene meeting photocatalysis: opportunities and challenges. Nano Energy 35:79–91
17. Zhang QE, Zhou AA, Wang JJ, Wu JF, Bai H (2017) Degradation-induced capacitance: a new insight into the superior capacitive performance of polyaniline/graphene composites. Energy Environ Sci 10:2372–2382
18. Al-Amri AM, Cheng B, He JH (2019) Perovskite methylammonium lead trihalide heterostructures: progress and challenges. IEEE Trans Nano 18:1–12
19. Alarawi A, Ramalingam V, He JH (2019) Recent advances in emerging single atom confined two-dimensional materials for water splitting applications. Mater Today Energy 11:1–23
20. Liu MC, Xu Y, Hu YX, Yang QQ, Kong LB, Liu WW, Niu WJ, Chueh YL (2018) Electrostatically charged MoS2/graphene oxide hybrid composites for excellent electrochemical energy storage devices. ACS Appl Mater Interfaces 10(41):35571–35579
21. Tang SY, Medina H, Yen YT, Chen CW, Yang TY, Wei KH, Chueh YL (2019) Enhanced photocarrier generation with selectable wavelengths by M-decorated-$CuInS_2$ nanocrystals (M = Au and Pt) synthesized in a single surfactant process on MoS_2 bilayers. Small 15:1803529
22. Chen C, Wang XF, Li YS, Cheng XM, Yao AL (2017) Single-band negative differential resistance in metallic armchair MoS2 nanoribbons. J Phys D 50: 465302
23. Yao AL, Wang XF, Liu YS, Sun YN (2018) Electronic structure and I-V characteristics of InSe nanoribbons. Nanoscale Res Lett 13:107
24. Llinas JP, Fairbrother A, Barin GB, Shi W, Lee K, Wu S, Choi BY, Braganza R, Lear J, Kau N, Choi W, Chen C, Pedramrazi Z, Dumslaff T, Narita A, Feng XL, Müllen K, Fischer F, Zettl A, Ruffieux P, Yablonovitch E, Crommie M, Fasel R, Bokor J (2017) Short-channel field-effect transistors with 9-atom and 13-atom wide graphene nanoribbons. Nat Comm 8:633
25. Liu YY, Xiao H, Goddard WA III (2016) Schottky-barrier-free contacts with two-dimensional semiconductors by surface-engineered MXenes. J Am Chem Soc 138:15853–15856
26. Hu W, Lin L, Yang C, Dai J, Yang JL (2016) Edge-modified phosphorene nanoflake heterojunctions as highly efficient solar cells. Nano Letters 16: 1675–1682
27. Hong JH, Jin CH, Yuan J, Zhang Z (2017) Atomic defects in two-dimensional materials: from single-atom spectroscopy to functionalities in opto-/electronics, Nanomagnetism, and Catalysis. Adv Mater 29:1606434
28. Li XF, Puretzky AA, Sang XH, Santosh KC, Tian MK, Ceballos F, Mahjouri-Samani M, Wang K, Unocic RR, Zhao H, Duscher G, Cooper VR, Rouleau CM, Geohegan DB, Xiao K (2017) Suppression of defects and deep levels using isoelectronic tungsten substitution in monolayer $MoSe_2$. Adv Funct Mater 27:1603850
29. Zhai MX, Wang XF, Vasilopoulos P, Liu YS, Dong YJ, Zhou LP, Jiang YJ, You WL (2014) Giant magnetoresistance and spin Seebeck coefficient in zigzag α-graphyne nanoribbons. Nanoscale 6:11121–11129
30. Liu F, Zhou JD, Zhu C, Liu Z (2016) Electric field effect in two-dimensional transition metal dichalcogenides. Adv Funct Mater 27:1602404
31. Jariwala D, Marks TJ, Hersam MC (2017) Mixed-dimensional van der Waals heterostructures. Nature Materials 16:170–181
32. Gao AY, Lai JW, Wang YJ, Zhu Z, Zeng JW, Yu GL, Wang NZ, Chen WC, Cao TJ, Hu WD, Sun D, Chen XH, Miao F, Shi Y, Wang XM (2019) Observation of ballistic avalanche phenomena in nanoscale vertical InSe/BP heterostructures. Nature Nanotech 14:217–222

33. Tran V, Soklaski R, Liang YF, Li Y (2014) Layer-controlled band gap and anisotropic excitons in few-layer black phosphorus. Phys Rev B 89:235319
34. Liu H, Neal AT, Zhu Z, Luo Z, Xu XF, Tománek D, Ye PD (2014) Phosphorene: an unexplored 2D semiconductor with a high hole mobility. Acs Nano 8: 4033–4041
35. Qiao JS, Kong XH, Hu ZX, Yang F, Ji W (2014) Few-layer black phosphorus: emerging 2D semiconductor with high carrier mobility and linear dichroism. Nat Commun 5:4475
36. Xia F, Wang H, Jia Y (2014) Rediscovering black phosphorus as an anisotropic layered material for optoelectronics and electronics. Nat Commun 5:4458
37. Liu C, Sun Z, Zhang L, Lv J, Yu XF, Zhang L, Chen X (2018) Black phosphorus integrated tilted fiber grating for ultrasensitive heavy metal sensing. Sens Actuators B Chem 257:1093–1098
38. Ren XH, Zhou J, Qi X, Liu YD, Huang ZY, Li ZJ, Ge YQ, Dhanabalan SC, Ponraj JS, Wang SY, Zhong JX, Zhang H (2017) Few-layer black phosphorus nanosheets as electrocatalysts for highly efficient oxygen evolution reaction. Advanced Energy Materials 7:1700396
39. Sun J, Sun YM, Pasta M, Zhou GM, Li YZ, Liu W, Xiong F, Cui Y (2016) Entrapment of polysulfides by a black-phosphorus-modified separator for lithium-sulfur batteries. Adv Mater 28:9797–9803
40. Carvalho A, Rodin AS, Neto AHC (2014) Phosphorene nanoribbons. Europhys Lett 108:47005
41. Guo HY, Lu N, Dai J, Wu XJ, Zeng XC (2014) Phosphorene nanoribbons, phosphorus nanotubes, and van der Waals multilayers. J Phys Chem C 118: 14051–14059
42. Amini M, Soltani M, Sharbafiun M (2019) Vacancy-induced Fano resonances in zigzag phosphorene nanoribbons. Phys Rev B 99:085403
43. Hashmi A, Hong J (2015) Transition metal doped phosphorene: first-principles study. J Phys Chem C 119:9198–9204
44. Babar R, Kabir M (2016) Transition metal and vacancy defect complexes in phosphorene: a spintronic perspective. J Phys Chem C 120:14991–15000
45. Chen N, Wang YP, Mu YW, Fan YF, Li SD (2017) A first-principles study on zigzag phosphorene nanoribbons passivated by iron-group atoms. Phys Chem Chem Phys 19:25441–25445
46. Li X, Yang J (2016) First-principles design of spintronics materials. National Science Review 3:365–381
47. Brown A, Rundqvist S (2010) Refinement of the crystal structure of black phosphorus. Acta Crystallographica 19(4):684–685
48. Li W, Zhang G, Zhang YW (2014) Electronic properties of edge-hydrogenated phosphorene nanoribbons: a first-principles study. J Phys Chem C 118:22368–22372
49. Han XY, Stewart HM, Shevlin SA, Catlow CRA, Guo ZX (2014) Strain and orientation modulated bandgaps and effective masses of phosphorene nanoribbons. Nano Letters 14:4607–4614
50. Datta S (2005) Quantum transport: atom to transistor. Cambridge University Press, Cambridge
51. Brandbyge M, Mozos JL, Ordejón P, Taylor J, Stokbro K (2002) Density-functional method for nonequilibrium electron transport. Phys Rev B 65: 165401
52. Taylor J, Guo H, Wang J (2001) Ab initio modeling of quantum transport properties of molecular electronic devices. Phys Rev B 63:245407
53. Ramasubramaniam A, Muniz AR (2014) Ab initio studies of thermodynamic and electronic properties of phosphorene nanoribbons. Phys Rev B 90: 085424
54. Guimarães MHD, Zomer PJ, Ingla-Aynés J, Brant JC, Tombros N, Wees BJ (2014) Controlling spin relaxation in hexagonal BN-encapsulated graphene with a transverse electric field. Phys Rev Lett 113:086602
55. Dolui K, Pemmaraju CD, Sanvito S (2012) Electric field effects on armchair MoS2 nanoribbons. ACS Nano 6:4823–4834
56. Guo ZN, Chen S, Wang ZZ, Yang ZY, Liu F, Xu YH, Wang JH, Yi Y, Zhang H, Liao L, Chu PK, Yu XF (2017) Metal-ion-modified black phosphorus with enhanced stability and transistor performance. Adv. Mater. 29:1703811
57. Zeng MQ, Tan LF, Wang LX, Mendes RG, Qin ZH, Huang YX, Zhang T, Fang LW, Zhang YF, Yue SL, Rümmeli MH, Peng LM, Liu ZF, Chen SL, Fu L (2016) Isotropic growth of graphene toward smoothing stitching. ACS Nano 10: 7189–7196
58. Zhang YF, Zhang Y, Li G, Lu JC, Que YD, Chen H, Berger R, Feng XL, Müllen K, Lin X, Zhang YY, Du SX, Pantelides ST, Gao HJ (2017) Sulfur-doped graphene nanoribbons with a sequence of distinct band gaps. Nano Research 10(10):3377–3384